Chapter 4

AGN "effervescent" heating, convection and thermal conduction in galaxy groups and clusters

---

[1] This chapter is based on two papers: Roychowdhury, S. et al., 2004, ApJ, 615, 681 and Roychowdhury, S. et al., 2005, submitted to ApJ.

Summary and the main results of chapter 4

Recent X-ray observations of clusters of galaxies have shown that the entropy of the intracluster medium (ICM), even at radii as large as half the virial radius, is higher than that expected from gravitational processes alone. This is thought to be the result of non-gravitational processes influencing the physical state of the ICM. In this chapter, we investigate whether heating by buoyant bubbles from a central AGN can explain the distribution of excess entropy as a function of radius. The AGN is assumed to inject buoyant bubbles into the ICM, which heat the ambient medium by doing pdV work as they rise and expand. Several authors have suggested that this "effervescent heating" mechanism could allow the central regions of clusters to avoid the "cooling catastrophe". Here we study the effect of effervescent heating at large radii. In this model, we also include convection to arrive at entropy profiles of the intracluster gas which did not have any unphysical negative gradient in the central regions which would make the gas convectively unstable. This was prompted by the fact that observations of cluster gas never show such negative entropy gradients. In this chapter, we also investigate in detail the effects of thermal conduction when the cluster gas is heated by a central AGN by "effervescent heating" mechanism. Thermal conduction is known to be an important physical process for gas in galaxy clusters. In this context, it turns out to be important since AGN heating gives rise to large negative temperature gradients which can be removed efficiently by thermal conduction. The main results of these two models are

- ***The predictions of this model which involve AGN heating and covection is seen to be mainly sensitive to the total energy injected into the cluster.***
- ***We show that such a heating mechanism is able to solve the entropy problem, provided the total energy injected by AGN is roughly proportional to the cluster mass.***
- ***Convection is seen to remove unphysical, negative entropy gradients in the central regions of clusters. An isentropic core is seen to develop in the central regions of the cluster. The temperature profiles still are seen to have a negative gradient in the central regions.***
- ***The cluster profiles of density, temperature and entropy resulting from the evolution of the ICM with AGN heating, thermal conduction and radiative cooling are seen to be better consistent with observations.***
- ***Unlike previously proposed preheating models, our model with thermal conduction predicts that isentropic cores are not an inevitable consequence of preheating. The model also reproduces the observational trend for the density profiles to flatten in lower mass systems.***
- ***We deduce the energy required to explain the entropy observations as a function of mass of groups and clusters for this model with AGN heating and thermal conduction. We show that the entropy measurements, in conjunction with our model, place constraints on the cluster—black hole mass relation.***

4.1 Introduction

Recent X-ray observations of both rich and poor clusters of galaxies have shown that there are problems in understanding the temperature, gas density or, equivalently, the entropy profiles at large radii ($\sim 0.5 r_{\rm vir}$, where $r_{\rm vir}$ is the virial radius) (Ponman et al. 2003). The observed entropy at $0.1 r_{200}$ and at r_{500} (where r_{200} and r_{500} correspond to radii within which the average overdensity is 200 and 500, respectively) is higher than that estimated from the purely gravitational interaction of gas with dark matter (Ponman et al. 2003 and references therein; see also Roychowdhury & Nath 2003). Earlier X-ray observations by Lloyd-Davies et al. (2000) had shown that entropy at $0.1 r_{200}$ reached a "floor" for poor clusters and groups. However, recent results of Ponman et al. (2003) have shown that the observed entropy is higher than the gravitational expectations for all clusters with emission-weighted temperatures $\langle T \rangle$ in the range 1 – 10 keV. The entropy at the much larger radius of r_{500} is also found to be higher than expected from purely gravitational processes.

Many theoretical models have been proposed to explain this phenomenon, including models that involve heat input from supernovae (Valageas & Silk 1999; Wu, Nulsen & Fabian 2000), gas cooling (Bryan 2000; Voit & Bryan 2001; Muanwong et al. 2002; Wu & Xue 2002; Davé, Katz & Weinberg 2002, Tornatore et al. 2003), accretion shocks (Tozzi & Norman 2001; Babul et al. 2002) and quasar outflows (Nath & Roychowdhury 2002). More information on various heating models can be found in a review by Gardini & Ricker (2004).

Observations have also revealed the presence of X-ray deficient bubbles in the inner regions of many cooling flow clusters, e.g., the Hydra A cluster (McNamara et al. 2000), Abell 2052 (Blanton et al. 2001, 2003), Abell 2597 (McNamara et al. 2001), Abell 4059 (Heinz et al. 2002), Abell 2199 (Johnstone et al. 2002), and others. These bubbles are characterized by low X-ray emissivity, implying low density compared to the ambient medium. In most of these cases, the cavities are clearly coincident with the radio lobes of the AGN in the cluster center. However, some clusters also exhibit cavities with weak or undetectable radio emission (known as "ghost bubbles" or "ghost cavities") located far away from the cluster centers, like Perseus (Fabian et al. 2000), MKW3s (Mazzotta et al. 2002), and Abell 2597 (McNamara et al. 2001). These bubbles are also believed to be filled with relativistic plasma or buoyant gas deposited by jets from the central AGN, and are thought to rise through the ICM subsonically due to buoyancy. As they rise, radiative and adiabatic losses reduce the energy of the relativistic plasma inside the bubbles, resulting in a very low radio flux. The discovery of these bubbles and their detailed observational study have stimulated theoretical studies of the impact of these bubbles on the intracluster medium.

The evolution of these bubbles has been studied extensively in connection with the cooling flow catastrophe in the centers of clusters. It has been found recently that simple cooling flow model of clusters, which predict that the temperature of gas in the central regions of clusters should be very low (much less than 1 keV), are mostly in conflict with the observed temperature profiles (Peterson et al. 2001; Allen et al. 2001 and many others). Several authors have addressed whether the absence of very cold gas (below $\sim$ 1 keV) can be explained by AGN energy input via outflows and bubbles (see, e.g., Tabor & Binney 1993, Binney & Tabor 1995, Ruszkowski & Begelman 2002, Churazov et al. 2002, Kaiser & Binney 2003, and Brüggen 2003a for semi-analytic models; and Quilis et al. 2001, Reynolds et al. 2002, Brüggen 2003b, and Ruszkowski, Brüggen & Begelman 2004, Basson

& Alexander 2003, Omma et al. 2003a, Omma & Binney 2003b for numerical simulations).

In a recent study Croston et al. (2004) presented the luminosity-temperature relation for groups and separated the sample into "radio loud" or "quiet" objects. They showed that "radio loud" groups deviated more from the self-similar scaling than the radio quiet ones. [1] This argument adds more credibility to the idea that AGNs are responsible for the entropy "floor" and deviations from self-similar scalings.

In this chapter, we explore the possibility of heating the intracluster gas at large radii via the "effervescent heating" mechanism (Begelman 2001, Ruszkowski & Begelman 2002). Since the excess entropy requirements at different radii are different, the questions we set out to answer are the following:

1. Is it possible to satisfy simultaneously the entropy observations at two fiducial radii ($0.1r_{200}$ and at r_{500}) with a single central heating source for all clusters? We explore the parameter space in time-averaged jet luminosity $\langle L \rangle$ and the time for which this activity continues, $t_{\rm heat}$.

2. How does the entropy profile of the cluster gas evolve with time when it is being heated and cooled simultaneously?

Here we explore two models of AGN heating in clusters. In the first model, we study the evolution of the density, temperature and entropy profiles of the ICM under the effect of "effervescent heating" from buoyant bubbles in the presence of radiative cooling and convection. In addition, we also explore another model where the effects of AGN heating in clusters is examined in the presence of thermal conduction and cooling.

The role of thermal conduction in the intracluster medium has generated a lot of interest in recent times. Its role, however, has mostly been discussed or studied in detail in reference to cooling flows in the central regions of clusters. Many authors have investigated whether thermal conduction alone can act as a heating source in the centre of clusters to stop the gas from radiatively cooling to very low temperatures (e.g., Zakamska & Narayan, 2003; Voigt et al. 2002; Loeb 2002). It has also been studied along with other heating mechanisms like "effervescent heating" again in the context of cooling flows in the centers of clusters (Ruszkowski & Begelman, 2002). In this chapter, we study the effect of thermal conduction along with heating via AGN in changing the entropy and temperature profiles of the ICM.

The chapter is organized as follows. In § 2 we describe both our models: firstly, "effervescent heating" with convection, including initial conditions, details of the effervescent heating mechanism, our prescriptions for cooling and convection (models (A1) and (A2)), and the simulation method; next "effervescent heating" with thermal conduction and all other relevant details of the model. The results of all three models are presented in § 3. The discussions of the three models (A1), (A2) and (B) are presented in §§ 4 and 5, respectively. Some caveats of these models are discussed in § 6. Finally, our conclusions are summarized in § 7.

[1] The extrapolation of the cluster L-T relation onto Figure 2 of Croston et al. (2004) would fall above all the points. Slightly smaller deviation in the radio quiet AGN could be due to the fact that they are not active now but were active in the past (see Donahue (2005))

4.2 Models of the intracluster medium

In this section, we first describe our model of the ICM with AGN heating, cooling and convection (model (A)). This model of the intracluster medium has two variations: model (A1) where the cluster has a pure NFW dark matter distribution and where the "effervescent" heating mechanism has been considered without considering any loss of AGN energy due to bubble creation and model (A2) where the cluster has a smoothened NFW profile with a core in the centre and where the energy loss due to bubble creation has also been taken into account while heating the ICM.

Our model of the cluster gas assumes that the ICM remains in hydrostatic equilibrium as it is heated by buoyant radio bubbles, originating from the central AGN, via the "effervescent heating" mechanism.

4.2.1 Model (A1): Pure NFW dark matter distribution and *no* energy loss due to bubble creation

We begin the description of model (A1) with a description of the background dark matter potential of the cluster.

4.2.1.1 Dark matter density profile

We assume that the dark matter density profile of the cluster, $\rho_{\rm dm}(r)$, is described by a self-similar form as suggested by many high resolution N-body simulations. The profile is expressed in terms of a characteristic radius, $r_{\rm s}$, by

$$\rho_{\rm dm}(r) = \frac{\rho_s}{x(1+x)^2} \tag{4.1}$$

(see, e.g., Komatsu & Seljak 2002), where $\rho_{\rm s}$ is a characteristic density and $x = r/r_{\rm s}$. We define a dimensionless "concentration parameter" $c \equiv r_{\rm vir}/r_{\rm s}$, where the virial radius $r_{\rm vir}$ is calculated from the spherical collapse model (Peebles 1980) assuming overdensity $\Delta_{\rm c}(z=0) = 100$ (Komatsu & Seljak 2002). The characteristic density $\rho_{\rm s}$ is then given by

$$\rho_{\rm s} = c^3 \frac{M_{\rm vir}}{4\pi r_{\rm vir}^3}\Big[\ln(1+c) - \frac{c}{(1+c)}\Big]^{-1}, \tag{4.2}$$

where $M_{\rm vir}$ is the cluster virial mass. The concentration parameter c can be approximated by

$$c = 9\Big(\frac{M_{\rm vir}}{1.5\times10^{13}h^{-1}M_\odot}\Big)^{-0.13}, \tag{4.3}$$

according to numerical simulations by Bullock et al. (2001) (we use $h = 0.71$).

The above set of equations specifies the dark matter density profile of a particular cluster as a function of its virial mass. Next, we turn our attention to the density profile of the gas in hydrostatic equilibrium with this dark matter distribution.

To compare our results with observations, we present our results in terms of the radii r_{200} and r_{500}, where the overdensities are 200 and 500, respectively. Both radii functions of the cluster mass. The ratio $r_{500}/r_{200} \approx 0.65 - 0.67$ for the range of masses we have considered.

4.2.1.2 Initial configuration of intracluster gas

We use the "universal temperature profile" (Loken et al. 2002) as the initial temperature profile of gas in hydrostatic equilibrium to determine the initial density profile. This profile is different from the commonly used self-similar profile, which assumes that the intracluster gas density distribution scales as the dark matter density profile with a constant of proportionality $f_{\rm b} = \Omega_{\rm b}/\Omega_{\rm m}$ (i.e., $\rho_{\rm gas} = f_{\rm b}\rho_{\rm dm}$). We use the "universal temperature profile" instead of the self-similar profile because the former is claimed to be the result of gravitational processes alone. Moreover, it does not have the unrealistic turnover of the temperature profile in the inner regions of the cluster, which one finds in the self-similar profile (see chapter (2) and Roychowdhury & Nath 2003 for details).

The initial temperature profile (normalized by the emission-weighted temperature $\langle T \rangle$), in the radial range $0.04 r_{\rm vir} \leq r \leq r_{\rm vir}$, is given by

$$\frac{T_o(r)}{\langle T \rangle} = \frac{b}{(1 + r/a)^{\delta}} \tag{4.4}$$

where $b = 1.33$, $a = r_{\rm vir}/1.5$, and $\delta = 1.6$. To determine the emission-weighted temperature from the cluster mass, we use a relation that arises from adiabatic evolution of the gas in the cluster. Afshordi & Cen (2002) have shown that the observations by Finoguenov et al. (2001) of the M_{500}–$\langle T \rangle$ relation in clusters can be understood from gravitational processes alone. We therefore use this empirical relation (M_{500}–$\langle T \rangle$) derived by Finoguenov et al. (2001):

$$M_{500} = 2.64 \times 10^{13} \Big(\frac{k_{\rm b} \langle T \rangle}{1 \ {\rm keV}} \Big)^{1.78} {\rm M}_{\odot}, \tag{4.5}$$

where $k_{\rm b}$ is the Boltzmann constant and M_{500} has been calculated self-consistently by taking the total mass within the radius where the overdensity is $\delta \geq 500$.

The equation of hydrostatic equilibrium for gas in a cluster with temperature $T(r)$ and density $\rho_{\rm gas0}(r)$ is

$$\frac{1}{\rho_{\rm gas0}(r)} \frac{d}{dr} (P_{\rm gas0}(r)) = -\frac{GM(\leq r)}{r^2}, \tag{4.6}$$

where $P_{\rm gas0} = (\rho_{\rm gas0}/\mu m_{\rm p}) k_{\rm b} T_0$, $M(\leq r)$ is the total mass inside radius r, and μ and $m_{\rm p}$ denote the mean molecular weight ($\mu = 0.59$) and the proton mass, respectively. The boundary condition imposed on the solution is that the gas-fraction, $f_{\rm gas} \equiv M_{\rm gas}/M_{\rm dm} = 0.13333$, within r_{200} is universal, as recently found by Ettori (2003) for a sample of low- and high-redshift clusters.

4.2.1.3 Effervescent heating and radiative cooling

In the "effervescent heating" model, the central AGN is assumed to inflate buoyant bubbles of relativistic plasma in the ICM (Begelman 2001, Ruszkowski & Begelman 2002). The timescale for the bubbles to cross the cluster (of order the free-fall time) is shorter than the cooling timescale. Since the number flux of bubbles is large, the flux of bubble energy through the ICM approaches a steady state. This implies that details of the energy injection process such as the number flux of bubbles, the bubble radius or size, filling factor and rate of rise do not affect the average heating rate.

It is assumed that the relativistic gas does not mix with the ICM very efficiently. Under such conditions the bubbles can expand and do pdV work on the ambient medium as they rise in the

cluster pressure gradient. We assume that this work converts internal energy of the bubbles to thermal energy of the intracluster gas within a pressure scale height of where it is generated. Then, in a steady state (and assuming spherical symmetry), the energy flux carried by the bubbles varies as

$$F_{\rm b} \propto \frac{P_{\rm b}(r)^{(\gamma_{\rm b}-1)/\gamma_{\rm b}}}{r^2} \tag{4.7}$$

where $P_{\rm b}(r)$ is the partial pressure of buoyant gas inside the bubbles at radius r and $\gamma_{\rm b}$ is the adiabatic index of buoyant gas, which we have taken to be 4/3. This formula includes the effects of adiabatic bubble inflation. Assuming that the partial pressure inside these bubbles scales as the thermal pressure of the ICM, the volume heating function $\mathcal{H}$ can be expressed as

$$\begin{aligned} \mathcal{H} &\sim -r^2 h(r) \nabla \cdot (\hat{\mathbf{r}} F_{\rm b}) \\ &= -h(r) \Big(\frac{P_{\rm gas}}{P_0}\Big)^{(\gamma_{\rm b}-1)/\gamma_{\rm b}} \frac{1}{r} \frac{d \ln P_{\rm gas}}{d \ln r}, \end{aligned} \tag{4.8}$$

where P_0 is some reference pressure and $h(r)$ is the normalization function

$$h(r) = \frac{\langle L \rangle}{4\pi r^2} (1 - \exp(-r/r_0))\, q^{-1}. \tag{4.9}$$

In equation (4.9), $\langle L \rangle$ is the time-averaged energy injection rate and r_0 is the inner heating cut-off radius which is determined by the size of the central heating source. In our calculations r_0 is taken to be $0.01 r_{\rm vir}$, which is $\sim 15 - 20$ kpc depending on the cluster mass $M_{\rm cl} (\equiv M_{\rm vir})$. The normalization factor q is defined by

$$q = \int_{r_{\rm min}}^{r_{\rm max}} \Big(\frac{P}{P_0}\Big)^{(\gamma_{\rm b}-1)/\gamma_{\rm b}} \frac{1}{r} \frac{d \ln P}{d \ln r} (1 - \exp(-r/r_0))\, dr, \tag{4.10}$$

where $r_{\rm max} = r_{200}$.

To calculate the volume cooling rate, we use a fit to the normalized cooling function $\Lambda_{\rm N}(T)$ for a metallicity of $Z/Z_\odot = 0.3$, as calculated by Sutherland & Dopita (1993). This cooling function incorporates the effects of free-free emission and line cooling. The fit is borrowed from Nath (2003). Thus, the volume cooling rate is $\Gamma = n_{\rm e}^2 \Lambda_{\rm N}(T)$, where $n_{\rm e} = 0.875(\rho/m_{\rm p})$ is the electron density.

4.2.1.4 Convection

The convective flux $F_{\rm conv}$ is given by the mixing length theory,

$$F_{\rm conv} = \begin{cases} 2^{-5/2} c_{\rm p}^{-1/2} T g^{1/2} \rho_{\rm gas} l_{\rm m}^2 (-\nabla \hat{s})^{3/2} & \text{if } \nabla \hat{s} < 0, \\ 0 & \text{otherwise,} \end{cases} \tag{4.11}$$

where g is the gravitational acceleration, $l_{\rm m}$ is the mixing length, $\hat{s} = (\gamma - 1)^{-1} k_{\rm b}/(\mu m_{\rm p}) \ln(P_{\rm gas}/\rho_{\rm gas}^{\gamma})$ is the gas entropy per unit mass, and $c_{\rm p} = \gamma k_{\rm b}/[(\gamma - 1)\mu m_{\rm p}]$ is the specific heat per unit mass at constant pressure. We use $l_{\rm m} = \min[0.3 P_{\rm gas}/(\rho_{\rm gas} g), r]$, where r is the distance from the cluster center.

Next we describe our model of AGN heating and convection in clusters with a smoothened NFW dark matter distribution. In this model we also include the energy loss due to bubble creation while we incorporate AGN heating in clusters (model (A2)).

4.2.2 Model (A2): smoothened NFW profile and energy loss due to bubble creation in "effervescent" mechanism

We briefly describe the default or the initial state of the intracluster gas for this model. Next, we describe the changes in the "effervescent" heating mechanism we have incorporated in model (A2) (as compared to model (A1)) to take into account the loss in energy due to bubble creation.

4.2.2.1 The default state of the ICM

Recent simulations of Loken et al. (2002) show that the ICM assumes a "universal temperature profile" due to gravitational interactions with the dark matter potential. The temperature profile (normalized by the emission-weighted temperature $\langle T \rangle$), in the radial range $0.04 r_{\rm vir} \leq r \leq r_{\rm vir}$, is given by

$$\frac{T_o(r)}{\langle T \rangle} = \frac{b}{(1 + r/a)^{\delta}} \tag{4.12}$$

where $b = 1.33$, $a = r_{\rm vir}/1.5$, and $\delta = 1.6$.

Here, we have assumed that the default or initial state of the intracluster gas is given by the "universal temperature profile".

To determine the emission-weighted temperature from the cluster mass, we use a relation that arises from adiabatic evolution of the gas in the cluster. Afshordi & Cen (2002) have shown that the observations by Finoguenov et al. (2001) of the M_{500}–$\langle T \rangle$ relation in clusters can be understood from gravitational processes alone. We therefore use this empirical relation (M_{500}–$\langle T \rangle$) derived by Finoguenov et al. (2000).

$$M_{500} = 2.64 \times 10^{13} \Big(\frac{k_{\rm b} \langle T \rangle}{1 \ {\rm keV}} \Big)^{1.78} {\rm M}_{\odot}, \tag{4.13}$$

where $k_{\rm b}$ is the Boltzmann constant and M_{500} has been calculated self-consistently by taking the total mass within the radius where the overdensity is $\delta \geq 500$.

Next, assuming that the ICM is in hydrostatic equilibrium with the background dark matter potential (which is given by the universal self-similar Navarro, Frenk & White (NFW) profile; Komatsu & Seljak 2002), we evaluate its density profile (see chapter (2) for details). The boundary condition imposed here is $f_{\rm gas} \equiv M_{\rm gas}/M_{\rm dm} = 0.13333$, within r_{200} (where r_{200} corresponds to radii within which the average overdensity is 200) is universal, as recently found by Ettori (2003) for a sample of low- and high-redshift clusters.

The background dark matter density profile is given by the self-similar Navarro, Frenk & White (NFW) profile (Komatsu & Seljak 2001) with a softened core (Zakamska & Narayan, 2003);

$$\rho_{\rm dm} = \frac{\rho_{\rm s}}{(r + r_{\rm c})(r + r_{\rm s})^2} \tag{4.14}$$

Here, $r_{\rm s}$ is the standard characteristic radius of the NFW profile, $r_{\rm c}$ is a core radius inside which the density profile is a constant and $\rho_{\rm s}$ is the standard characteristic density of the usual NFW profile. We, define a dimensionless parameter, $x = r/r_{\rm s}$, following Komatsu & Seljak, 2001, and $x_{\rm c} = r/r_{\rm c}$. Thus, we can arrive at the mass profile which will also be universal,

$$M_{\rm dm}(\leq r) = 4\pi \rho_{\rm s} r_{\rm s}^3 m(x) \tag{4.15}$$

where $m(x)$ is a non-dimensional mass profile given by

$$\begin{aligned} m(x) &= \int_0^x \frac{x^2 dx}{(x + x_c/x)(1+x)^2} \\ &= \frac{x_c^2}{(1-x_c)^2} \ln(1 + x/x_c) \\ &\quad + \frac{(1-2x_c)}{(1-x_c)^2} \ln(1+x) - \frac{1}{1-x_c}\frac{x}{1+x} \end{aligned} \tag{4.16}$$

It should be noted here that if $r_c = 0$, the usual NFW density and mass distribution can be recovered as in Komatsu & Seljak, 2001.

The value of r_c is quite uncertain but we follow Zakamska & Narayan, 2003 and take it to be $r_c = r_s/20$. This is thought to be reasonable since cluster lensing studies suggest that the core radius can be ~ tens of kilo-parsecs (Tyson et al., 1998; Shapiro & Iliev, 2000).

Here we also keep $r_c = 0$ to recover the standard NFW profile to investigate the effect of this smoothening of the dark matter profile on our results.

Next, we describe the non-gravitational heating of the intracluster medium from a central AGN via the "effervescent heating" mechanism (Begelman, 2000).

4.2.2.2 Effervescent heating and cooling

The effervescent heating mechanism is a gentle heating mechanism from a central AGN in which the cluster gas at all radii is heated by buoyant bubbles of relativistic plasma produced from a central source (Begelman 2000, Ruszkowski & Begelman, 2001) (as described in §§§ (4.2.1.3). The average volume heating rate is only a function of the ICM pressure gradient and averages over details such as bubble size, filling factor and so on. It is given by

$$\mathcal{H} = -h(r)\Big(\frac{P_{\rm gas}}{P_0}\Big)^{(\gamma_b-1)/\gamma_b} \frac{1}{r}\frac{d\ln P_{\rm gas}}{d\ln r}, \tag{4.17}$$

where $P_{\rm gas}$ is the ICM pressure, γ_b is the adiabatic index of buoyant gas in the bubbles, P_0 is some reference pressure and $h(r)$ is the normalization function

$$h(r) = \frac{\langle L\rangle}{4\pi r^2}(1 - \exp(-r/r_0))\, q^{-1}. \tag{4.18}$$

In equation (4.18), $\langle L\rangle$ is the time averaged energy injection rate and r_0 is the inner heating cut-off radius. The normalization factor q is defined by

$$q = \int_{r_{\rm min}}^{r_{\rm max}} \Big(\frac{P}{P_0}\Big)^{(\gamma_b-1)/\gamma_b} \frac{1}{r}\frac{d\ln P}{d\ln r}(1 - e^{-r/r_0})\, dr, \tag{4.19}$$

where $r_{\rm max} = r_{200}$.

The inner heating cut-off radius, r_0, is the transition region from the bubble formation region to the buoyant (effervescent) phase. It can be determined self-consistently by taking into account energy losses due to bubble creation,

$$\int_{r=0}^{r=r0} 4\pi r^2 \mathcal{H}\, dr = \Big[\frac{(\gamma_b - 1)}{\gamma_b}\Big] \times \langle L\rangle = \frac{1}{4}\langle L\rangle \tag{4.20}$$

This comes from the fact that the energy lost within the radius r_0 due to bubble creation at constant pressure is P_0V_0 where V_0 is the volume of the bubble at the creation region or transition region, r_0, and P_0 is the pressure at that region. However, the energy lost due to bubble expansion ie. in the effervescent phase is

$$\int_{P_0}^{0} P_{\rm bubble} dV \tag{4.21}$$

To get the maximum energy available in this phase, we have set the upper limit of the integral to zero pressure. Assuming adiabatic evolution of the gas inside the bubbles (low density, low radiative losses) and mass conservation in the bubble one has $dV = (1/\gamma_{\rm b})(P_0/P_{\rm bubble})^{1/\gamma_{\rm b}} V_0\, dP/P$. On integrating, one gets effervescent energy as $3P_0V_0$ for $\gamma_{\rm b} = 4/3$. It can be easily seen from above that the energy loss due to bubble creation is approximately only 25% of the total energy available for heating. Thus this condition sets the inner cut-off radius, r_0, since this 25% of the total energy or, equivalently, $1/4\langle L\rangle$ will be lost for bubble creation and injection within this radius. We find that r_0 roughly comes out to be around $\simeq 20 - 45$ kpc depending on the cluster mass $M_{\rm cl}(\equiv M_{\rm vir})$ and also the time-step of evaluation.

In this model, radiative cooling is also implemented. This has already been described in the earlier model (A1). In addition to heating and radiative cooling, we also include convection which has already been described earlier in §§§ (4.2.2.4)

Finally we go on to describe our model of the ICM with heating, cooling and thermal conduction.

4.2.3 Model (B): Effervescent heating, cooling and thermal conduction

4.2.3.1 The default state of the ICM

The details of the initial conditions of model (B) are exactly similar to those adopted earlier in model (A2).

The effervescent heating mechanism and radiative cooling have been discussed already in §§§ (4.2.2.2).

4.2.3.2 Thermal Conduction

A potential difficulty in raising the entropy of the intracluster medium at large radii ($r > 0.1r_{200}$) by means of a central heating source is that the energy required is fairly large ($\gtrsim 10^{62}$ erg) over a period of the age of the cluster. This sets up a negative entropy gradient in the central regions of clusters (see right panel of Figure (4.2) and a rising temperature profile (see right panel of Figure (4.4) which are somewhat different from the observed temperature and entropy profiles. Our previous models (A1) and (A2), however, did not include the effect of thermal conduction which would have decreased the temperature gradient in the inner region and made it consistent with observations. We, therefore, include the effect of thermal conduction here to address these issues.

Thermal conduction has been invoked to be an important process in galaxy clusters for quite some time (Bertschinger & Meiksin 1986; Malyshkin 2001; Brighenti & Mathews 2002; Voigt et al. 2002; Fabian, Voigt & Morris 2002). However it is not clear as to how dominant it would be since magnetic fields would suppress the conduction co-efficient by a large amount from the classical Spitzer value. However, recent theoretical works by Narayan & Medvedev (2001), Chandran & Maron (2004), Loeb

(2002) and several others suggests that the suppression factor could be as high as 10% to 20% of the Spitzer value in the presence of a tangled and turbulent magnetic field. Motivated by these results we adopt the suppression factor $f = 0.1$.

The flux due to thermal conduction $F_{\rm cond}$ is given by

$$\mathbf{F}_{\rm cond} = -f\kappa\nabla T, \tag{4.22}$$

where κ is the Spitzer conductivity

$$\kappa = \frac{1.84\times10^{-5}T^{5/2}}{\ln\lambda}, \tag{4.23}$$

with the Coulomb logarithm $\ln\lambda = 37$, appropriate for ICM temperature and density.

4.2.4 Evolution of the intracluster gas

In this subsection, we describe the evolution of the ICM for all the three models (A1), (A2) and (B).

As noted earlier, the gas is assumed to be in quasi-hydrostatic equilibrium at all times since the cooling is not precipitous at these radii and the heating is mild. The gas entropy per particle is

$$S = const + \frac{1}{\gamma-1}k_{\rm b}\ln(\sigma). \tag{4.24}$$

where $\sigma \equiv P_{\rm gas}/\rho_{\rm gas}^{\gamma}$ is the "entropy index" and γ is the adiabatic index. The particle number density of the gas, n, is given by $n = \rho_{\rm gas}/\mu m_{\rm p}$.

During each timestep Δt, the entropy of a given mass shell changes by an amount

$$\Delta S = \frac{1}{\gamma-1}k_{\rm b}\frac{\Delta\sigma}{\sigma} = \frac{1}{nT}(\mathcal{H}-\Gamma-\nabla\cdot F_{\rm conv})\Delta t. \tag{4.25}$$

for models (A1) and (A2).

However, for model (B), equation (4.25) changes to

$$\Delta S = \frac{1}{\gamma-1}k_{\rm b}\frac{\Delta\sigma}{\sigma} = \frac{1}{nT}(\mathcal{H}-\Gamma-\nabla\cdot F_{\rm cond})\Delta t. \tag{4.26}$$

Incorporating the expressions for heating, cooling, and convection (models (A1) and (A2)), the entropy increment for each mass shell for a timestep Δt becomes

$$\begin{aligned}\Delta\sigma(M) = \frac{2}{3}\frac{\sigma}{P_{\rm gas}}\Delta t\Bigg[&-h(r)\Big(\frac{P_{\rm gas}}{P_0}\Big)^{(\gamma_{\rm b}-1)/\gamma_{\rm b}}\\ &\times\frac{1}{r}\frac{d\ln P_{\rm gas}}{d\ln r} - n_{\rm e}^2\Lambda_{\rm N}(T)\\ &-\frac{1}{r^2}\frac{d}{dr}(r^2F_{\rm conv})\Bigg]\end{aligned} \tag{4.27}$$

where $n_{\rm e}$ and $P_{\rm gas}$ are the current electron number density and pressure of the ICM, respectively.

Thus, the entropy index of each mass shell of gas due to heating and cooling after a time Δt becomes

$$\sigma_{\rm new}(M) = \sigma_0(M) + \Delta\sigma(M) \tag{4.28}$$

where $\sigma_0(M) = P_{\rm gas0}/\rho^{\gamma}_{\rm gas0}$ is the default entropy index. The system relaxes to a new state of hydrostatic equilibrium with a new density and temperature profile. After updating the function $\sigma(M)$ for each mass shell, we solve the equations

$$\frac{dP_{\rm gas}}{dM} = \frac{GM(\leq r)}{4\pi r^4} \tag{4.29}$$

$$\frac{dr}{dM} = \frac{1}{4\pi r^2}\Big(\frac{P_{\rm gas}(M)}{\sigma(M)}\Big)^{(1/\gamma)} \tag{4.30}$$

to determine the new density and temperature profiles at time $t+\Delta t$. The boundary conditions imposed on these equations are that (1) the pressure at the boundary of the cluster, $r_{\rm out}$, is constant and is equal to the initial pressure at r_{200}, i.e., $P\,(r_{\rm out})$ = constant = $P_{\rm gas0}(r_{200})$, and (2) the gas mass within $r_{\rm out}$ at all times is the mass contained within r_{200} for the default profile at the initial time, i.e., $M_{\rm g}(r_{\rm out}) = M_{\rm g0}(r_{200}) = 0.1333 M_{\rm dm}(r_{200})$ (Ettori 2003). It is important to note here that $r_{\rm out}$ increases as the cluster gas gets heated and spreads out.

The observed gas entropy $\mathcal{S}(r)$ at $0.1r_{200}$ and at r_{500} is then calculated using

$$\mathcal{S}(r) \equiv T(r)/n_{\rm e}^{2/3}(r). \tag{4.31}$$

The updated values of $\sigma(M)$ and pressure of the ICM $P_{\rm gas}(r)$ are used to calculate the heating and cooling rates and the convective flux for the next time step. This is continued for a duration of $t_{\rm heat}$. After that the heating source is switched off, putting $\mathcal{H} = 0$. The cooling rate and convective flux continue to be calculated to update the function $\sigma(M)$ at subsequent timesteps, and the hydrostatic structure is correspondingly evolved for a duration of $t_{\rm H} - t_{\rm heat}$, where $t_{\rm H}$ is the Hubble time. Noted that $r_{\rm out}$ decreases during this time since the intracluster gas loses entropy and shrinks.

Similarly, for model (B), ie. with thermal conduction in place of convection, the same steps (from equation (4.27) to equation (4.31)) are repeated for a Hubble time, $t_{\rm H}$, with similar values of $t_{\rm heat}$ as used in model (A) to find the final evolved state of the intracluster gas.

The only free parameters in our calculation are the energy injection rate $\langle L\rangle$ and the time $t_{\rm heat}$ over which the "effervescent heating" of the ICM takes place. After evolving the gas for the total available time, $t_{\rm H} \sim 1.35 \times 10^{10}$ years, we check whether the entropy at $0.1r_{200}$ and r_{500} matches the observed values, and adjust parameters accordingly. In this way, we explore the parameter space of $\langle L\rangle$ and $t_{\rm heat}$ for different cluster masses so that the entropy (after 1.35×10^{10} years) at $0.1r_{200}$ and r_{500} matches the observed values.

For numerical stability of the code, the convection term is integrated using timesteps that satisfy the appropriate Courant condition. The Courant condition for convection is

$$\Delta t_{\rm conv} \leq \frac{1}{2} 2^{5/2} \sqrt{\gamma} \frac{(\Delta r)^{5/2}}{g^{1/2} l_{\rm m}^2}. \tag{4.32}$$

Similarly, the conduction term is integrated using timesteps that satisfy the appropriate Courant condition. The Courant condition for thermal conduction is

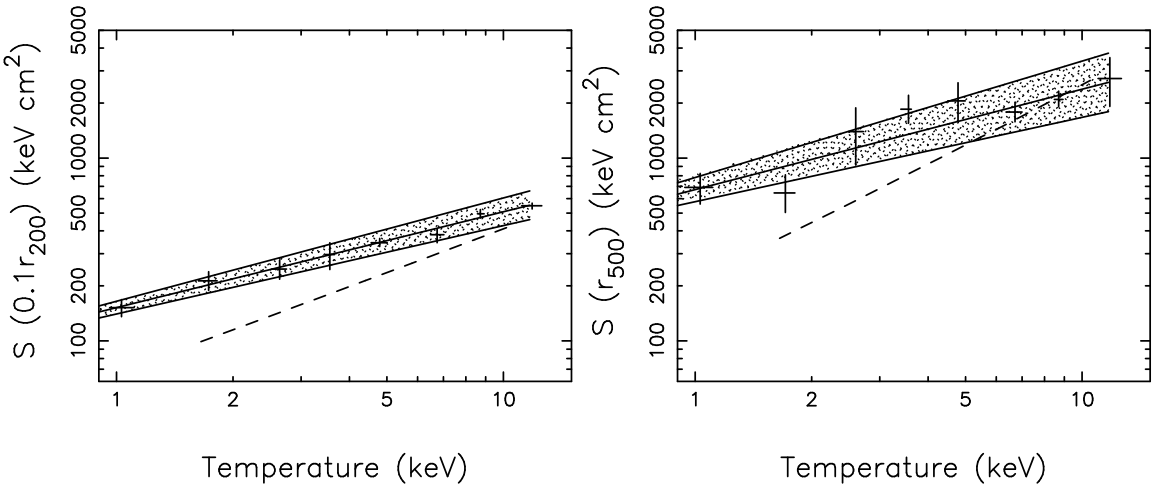

Figure 4.1: Gas entropy (defined here as $T/n_e^{2/3}$) as a function of emission-weighted temperature $\langle T \rangle$, at radii $0.1r_{200}$ (left panel) and r_{500} (right panel). The data points are from Ponman et al. (2003). The solid line in the center of the shaded region is the best-fit to the data points. The two solid lines bounding the shaded region are the $1-\sigma$ errors on the best-fit values of entropy. The dashed line is the predicted entropy due to gravitational interactions alone (from chapter (2)).

$$\Delta t_{\rm cond} \leq 0.5 \frac{(\Delta r)^2 n\, k_{\rm b}}{\kappa(\gamma-1)}. \tag{4.33}$$

The timesteps, Δt, used in equation (4.25) and equation (4.26) to update the entropy of the gas and calculate its obey the above Courant condition (Ruszkowski & Begelman 2002; Stone, Pringle & Begelman 1999).

The calculations presented in this chapter were also performed using the fully time-dependent *ZEUS* code (Clarke, Norman & Fiedler 1994) and the results obtained were consistent with the ones presented here. However, we decided to use our quasi-hydrostatic Lagrangian code as it allowed us to search the parameter space more efficiently.

4.3 Results

In this section, we discuss our results of cluster evolution for all three models (A1), (A2) and (B). The gas is heated for a time $t_{\rm heat}$ and cooled simultaneously. After this time, the heating source is switched off. The gas is then allowed to cool radiatively until a total simulation time of $t_{\rm H}$=1.35×10^{10} years has elapsed. The final entropy values at $0.1r_{200}$ and r_{500} are compared with the observed ones. In model (A1), ie. pure NFW profile and AGN heating with no loss due to bubble creation, convection and cooling, r_0 is fixed to $0.01r_{\rm vir}$ which is around $\simeq$ 15-20 kpc.

In Figure (4.1), the observed entropy values and their errors at $0.1r_{200}$ and at r_{500} are plotted as a function of the emission-weighted temperature, $\langle T \rangle$, of the cluster (Ponman et al. 2003). We have done a best-fit analysis on these data points to estimate the entropy requirements for the sample of clusters of masses ranging from 10^{14} to 2×10^{15} $M_\odot$. The results of our analysis are the shaded regions in the two panels of Figure (4.1). The solid line through the center of the shaded region is the best-fit curve with the lines bounding the shaded region being the $1-\sigma$ errors on the best-fit entropy values.

Figure (4.2) shows the time evolution of scaled entropy profiles of a cluster of mass $M_{\rm cl} = 6 \times 10^{14} M_{\odot}$ with and without convection for $\langle L \rangle = 3{\times}10^{45}$ erg s^{-1} for model (A1). We use the same method of emissivity weighting as used in chapter (2) to calculate the average quantities. The entropy profiles are plotted in time-steps of 5×10^8 years. They are seen to rise with time as the ICM is heated. Then, after the heating is switched off (after $t_{\rm heat} = 5 \times 10^9$ years), the gas loses entropy due to cooling and the profiles are seen to fall progressively until the Hubble time is reached. The inclusion of convection flattens the negative gradient in the scaled entropy profiles in the central regions of the cluster (within $0.2r_{200}$, as seen in the difference of the entropy profiles between the left and right panels in Figure (4.2). The plot that includes convection (left panel in Figure (4.2)) shows that the gas develops a flat entropy core in its central regions after the heating source has been switched off and the gas has cooled.

Left panel of Figure (4.3) shows the time evolution of scaled entropy profiles of a cluster of mass $M_{\rm cl} = 6 \times 10^{14} M_{\odot}$ for $\langle L \rangle = 3.0{\times}10^{45}$ erg s^{-1} for model (A2). The entropy profiles are plotted in time-steps of 5×10^8 years. They are seen to rise with time as the ICM is heated. Then, after the heating is switched off (after $t_{\rm heat} = 5{\times}10^9$ years), the gas loses entropy due to cooling and the profiles are seen to fall progressively. These entropy profiles here do not show a flat isentropic core in the central regions of the cluster, as compared to Figure (4.2) for model (A1). This is due to the inclusion of a smoothened core in the dark matter profile in this model. However, it is seen that the isentropic core develops for even higher mass clusters and for higher $\langle L \rangle$ though the radius of this core is smaller than that seen in model (A1)

Right panel of Figure (4.3) shows the time evolution of scaled entropy profiles of a cluster of mass $M_{\rm cl} = 6 \times 10^{14} M_{\odot}$ for $\langle L \rangle = 5.25{\times}10^{45}$ erg s^{-1} for model (B) ie. with thermal conduction and no convection. Again, we have used the same method of emissivity weighting as in chapter (2) to calculate the average quantities. The entropy profiles are plotted in time-steps of 5×10^8 years. They are seen to rise with time as the ICM is heated. Then, after the heating is switched off (after $t_{\rm heat} = 5{\times}10^9$ years), the gas loses entropy due to cooling and the profiles are seen to fall progressively. The inclusion of conduction removes the negative gradient in the scaled entropy profiles in the central regions of the cluster (within $0.5r_{200}$). These entropy profiles do not show any flat entropy core seen in model (A) (left panel in Figure (4.2)). Thus, this probably indicates that thermal conduction is a more plausible process in ICM than convection for such gentle AGN heating.

Figure (4.4) shows the evolution of density and temperature of the ICM for a cluster of mass $6 \times 10^{14}\ M_{\odot}$ and for a luminosity of $\langle L \rangle = 3 \times 10^{45}$ erg s^{-1} for model (A1). The gas density decreases with time during the heating epoch, and increases due to radiative cooling and convection after the heating source is switched off. It is interesting to note that the changes in density are minimal beyond $0.2r_{200}$, and that convection plays an important role in regulating the density profiles after the heating source is switched off for radii $r \leq 0.2r_{200}$. We note that for clusters with lower emission-weighted temperatures, the effects of heating and convection are seen at larger radii.

Figure (4.5) shows the evolution of density and temperature of the ICM for a cluster of mass $6 \times 10^{14}\ M_{\odot}$ and for a luminosity of $\langle L \rangle = 3 \times 10^{45}$ erg s^{-1} for model (A2). The gas density decreases with time during the heating epoch, and increases due to radiative cooling and convection after the heating source is switched off. It is interesting to note that the changes in density are minimal beyond $0.2r_{200}$, and that convection plays an important role in regulating the density profiles after the heating

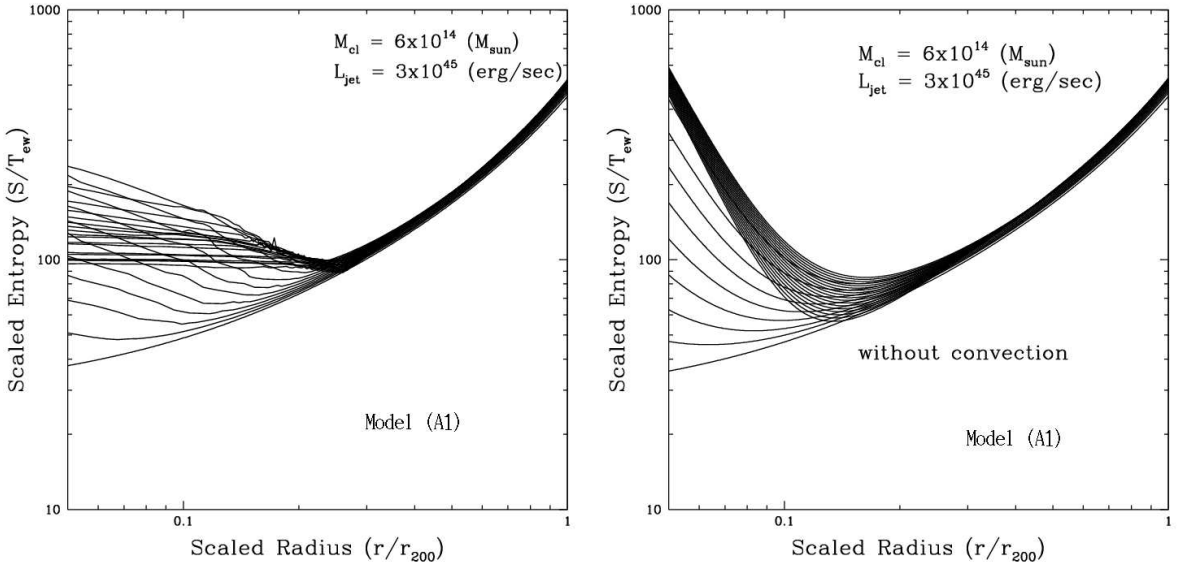

Figure 4.2: Scaled entropy profiles as a function of scaled radius for a cluster of mass $6 \times 10^{14}\ M_{\odot}$ heated by an AGN with $\langle L \rangle = 3 \times 10^{45}$ erg s^{-1}, with convection (left panel) and without convection (right panel) for model (A1). The scaled entropy profiles are plotted at intervals of $5{\times}10^{8}$ years. They are seen to rise as the gas is heated and then fall as the gas cools. In both cases $t_{\rm heat} = 5 \times 10^{9}$ years. Initial states correspond to the lowest curves.

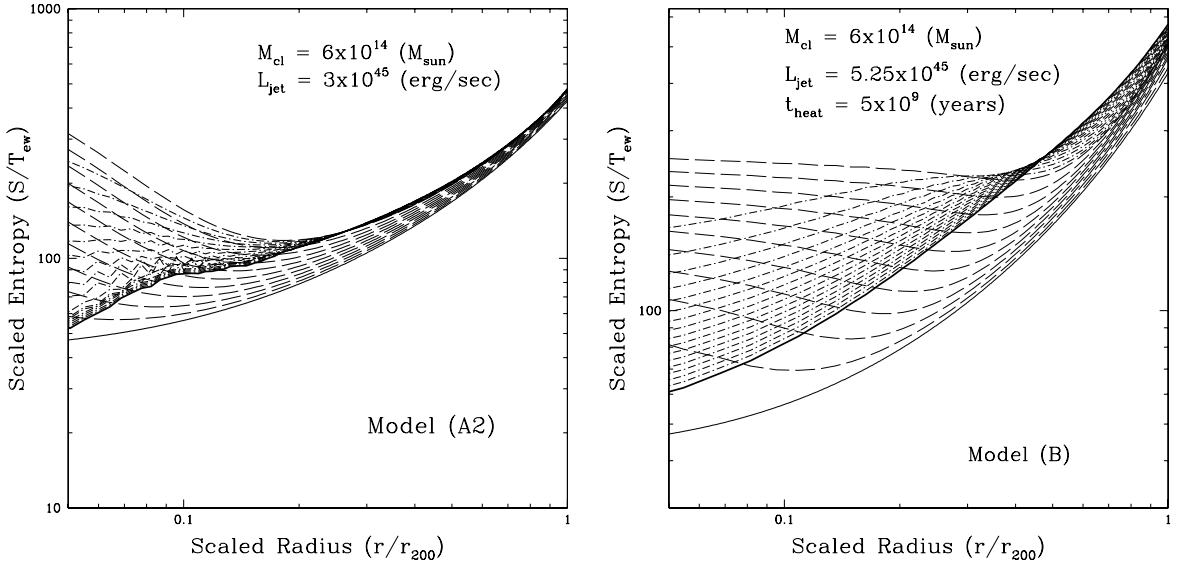

Figure 4.3: Scaled entropy profiles as a function of scaled radius for a cluster of mass $6 \times 10^{14}\ M_{\odot}$ heated by an AGN with $\langle L \rangle = 3.0 \times 10^{45}$ erg s^{-1} for model (A2) (left panel) and for model (B) where $\langle L \rangle = 5.25 \times 10^{45}$ erg s^{-1} (right panel). The scaled entropy profiles are plotted at intervals of $5{\times}10^{8}$ years. The dashed lines correspond to times when heating is on and the dot-dashed lines correspond to times when heating has been switched off. They are seen to rise as the gas is heated and then fall as the gas cools. It is seen here that the final entropy profiles (after Hubble time) has neither negative entropy gradient nor any entropy core in the central regions, as compared to Figure (4.2). Initial and final states correspond to the solid curves.

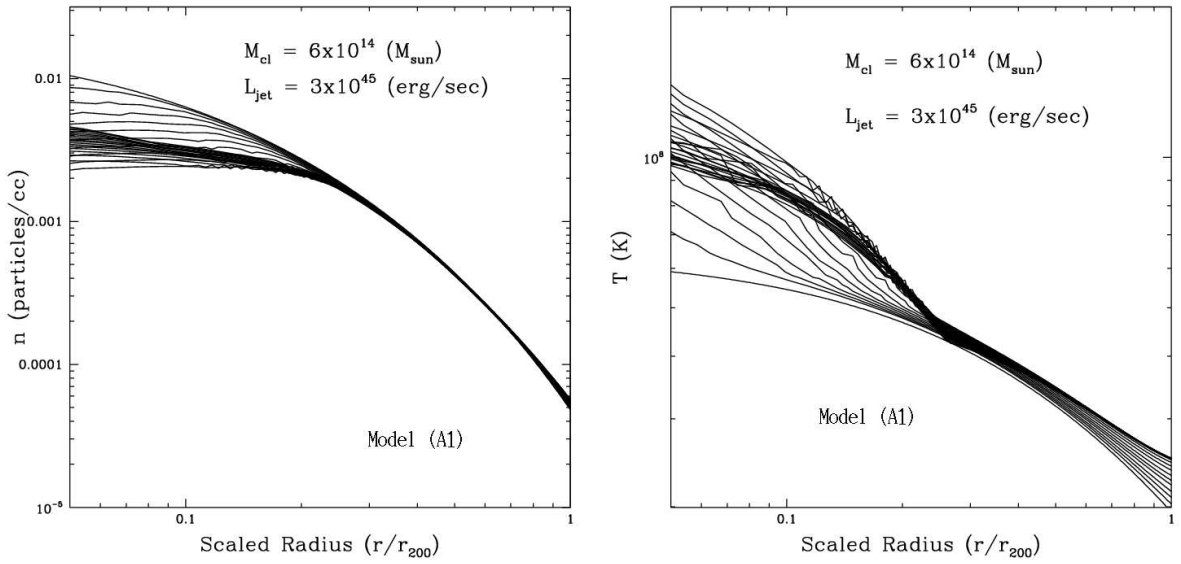

Figure 4.4: Gas density (left panel) and temperature (right panel) profiles as a function of scaled radius (r/r_{200}), for the cluster model (A1). It is seen here that radiative cooling lowers the temperature, thus increasing the density after the heating source is switched off. Initial density and temperature profiles correspond to the highest and lowest curves, respectively.

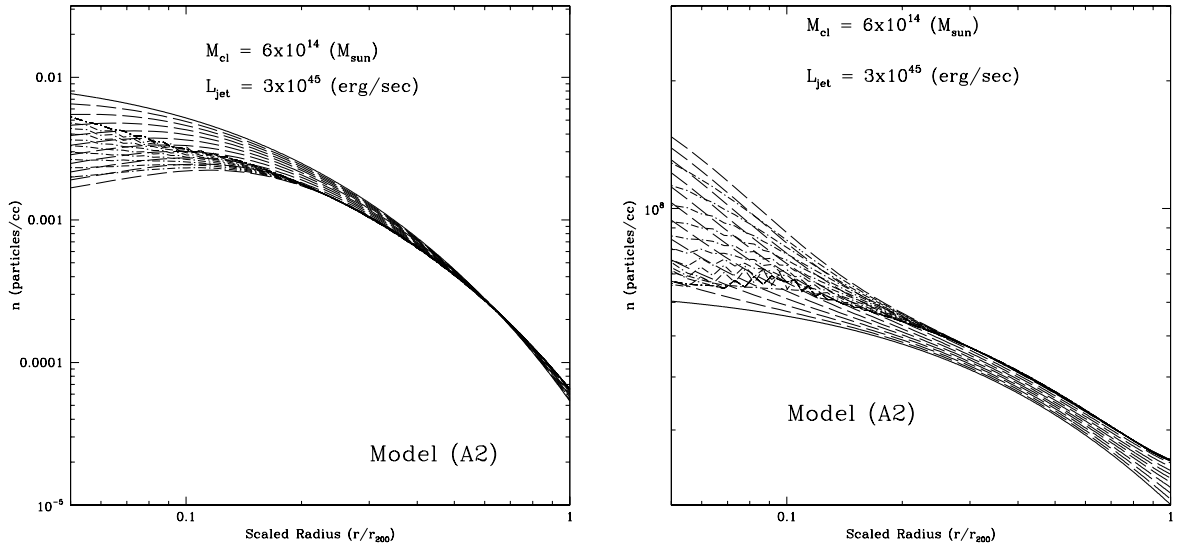

Figure 4.5: Gas density (left panel) and temperature (right panel) profiles as a function of scaled radius (r/r_{200}), for the cluster model (A2). It is seen here that radiative cooling lowers the temperature, thus increasing the density after the heating source is switched off. Initial density and temperature profiles correspond to the highest and lowest curves, respectively.

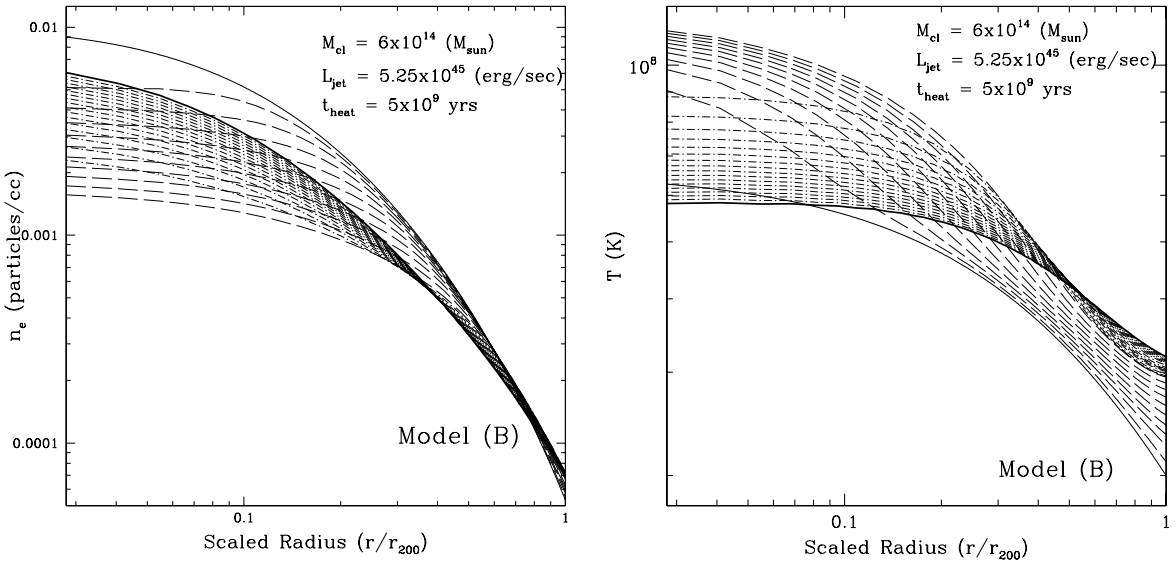

Figure 4.6: Gas density (left panel) and temperature (right panel) profiles as a function of scaled radius (r/r_{200}), for the cluster model (B) ie. AGN heating with thermal conduction and cooling. Dashed lines represent density profiles when heating is active and the dot-dashed line represents density profiles after the heating source has been switched off (i.e. after $t_{\rm heat} > 5 \times 10^9$ years). The profiles are plotted after every 5×10^8 years till Hubble time. It is seen here that conduction removes temperature gradients in the central regions (within $0.2r_{200}$) and flattens the temperature profile. This is the reason thermal conduction was included in the cluster model as compared to model (A1) and (A2), wherein left panel of Figure (4.4) shows rising temperatures in the centre. The density profiles are seen to rise after the heating source is switched off and thermal conduction and radiative cooling are the only two processes which are active. Initial density and temperature profiles correspond to the solid curves in both plots.

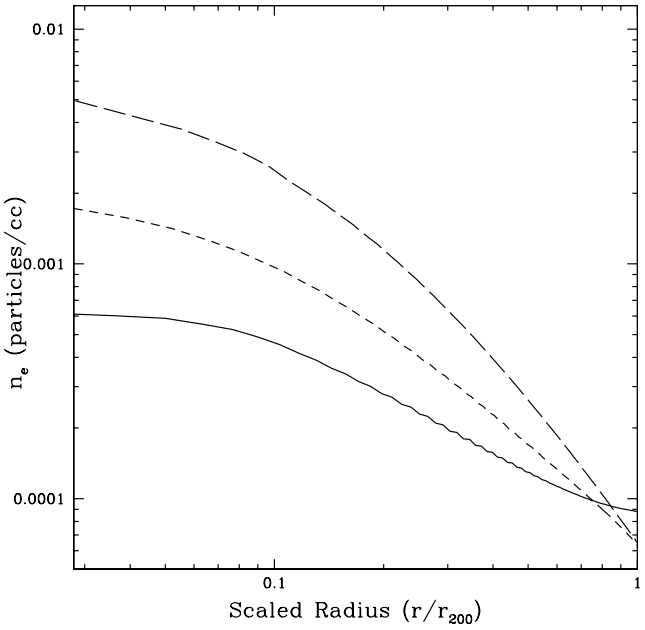

Figure 4.7: Final density profiles for objects of mass 4.5×10^{13} $M_\odot$ (solid line), 2.0×10^{14} $M_\odot$ (short dashed line), 9.0×10^{14} $M_\odot$ (long dashed line) for model (B) ie. AGN heating with thermal conduction. The assumed heating time $t_{\rm heat}$ in this example was 5×10^9 years. Note the flattening in the density profile as the mass of the system is decreased.

source is switched off for radii $r \leq 0.2r_{200}$, as noted in model (A1). We note that for clusters with lower emission-weighted temperatures, the effects of heating and convection are seen at larger radii. However, there is a slight difference in the temperature profiles seen here as compared to model (A1). The negative temperature gradient seen in the central regions in Figure (4.4) is almost non-existent in the left panel of Figure (4.5). This is probably because of the smoothening introduced in the dark matter profile in this model.

In Figure (4.6), the evolution of the density and temperature profiles of the ICM are shown for a cluster of mass 6×10^{14} $M_\odot$ and for a luminosity of $\langle L \rangle = 5.25 \times 10^{45}$ ergs^{-1} for the other model (B). The gas density decreases with time during the heating epoch, and increases due to radiative cooling and conduction after the heating source is switched off. It is interesting to note that the changes in density are minimal beyond $0.5r_{200}$, as compared to $0.2r_{200}$ in the left panel of Figure (4.4), and that conduction plays a very important role in regulating the density profiles after the heating source is switched off. It is seen that conduction actually decreases the density of the gas at larger radii (beyond $0.5r_{200}$) by conducting heat out from the central regions. This is seen more clearly if one studies the evolution of the temperature profiles. After the heating source is switched off, it is seen that the temperature of the central regions fall very rapidly since conduction pumps out heat from the central regions and redistributes it in the outer regions of the cluster. Thus the temperature profiles do not rise towards the centre as compared to what is seen in the right panel of Figure (4.4). On the other hand, their evolution shows a rise in the outer regions (beyond $0.5r_{200}$) due to thermal conduction even after the heat source has been switched off. Thus conduction acts like a heating source for larger radii.

Model (B) is constrained by entropy-temperature relation. At fixed cluster temperature this corresponds to a given density (at both radii for which the entropy data is provided). Now, since at a given density we have an additional constraint from the L-T relation (that our model fits reasonably well; see below), we implicitly satisfy the constraints on the slope of the density profile. Thus, as the model fits both the entropy data and the observed L-T relation that specify the slopes of the density profiles, these slopes must also be consistent with observations that show flattening in low mass systems. Indeed, this flattening is apparent in Figure (4.7) that shows final density profiles for different masses.

We now discuss the permitted range in the total energy injected into the cluster, $E_{\rm agn} = \langle L \rangle \times t_{\rm heat}$, required to match the observed entropy as a function of the cluster mass for all three models (A1), (A2) and (B). Figure (4.8) shows the spread in $E_{\rm agn}$ as a function of the cluster mass for two different values of $t_{\rm heat}$ for model (A). The region bounded by thin solid lines is the permitted range in energy for $t_{\rm heat}$ $= 5 \times 10^8$ years. This region includes an area shaded with solid vertical lines, which corresponds to the values of $E_{\rm agn}$ that satisfy the entropy requirement at $0.1r_{200}$, and another area shaded with solid oblique lines which satisfies the entropy requirement at r_{500}. Similarly, the region bounded by thin dotted lines in Figure (4.8) shows the permitted spread in energy for $t_{\rm heat} = 5 \times 10^9$ years. This region includes an area shaded with dots which corresponds to the values of $E_{\rm agn}$ that satisfy the entropy requirement at $0.1r_{200}$ and another area shaded with long-dashed horizontal lines, which satisfies the entropy requirement at r_{500}. For cluster masses above $9{\times}10^{14}M_{\odot}$ there is no lower limit on the injected energy from the entropy measurements at r_{500}. The region corresponding to this situation is marked by by horizontal dashed lines and oblique lines for cluster masses above $9 \times 10^{14}M_{\odot}$.

Top panels of Figure (4.9) show the permitted total injected energy range as a function of the mass of cluster for heating times between $t_{\rm heat} = 5 \times 10^8$ years and $t_{\rm heat} = 5 \times 10^9$ years for both models (A1) and (A2). The bottom panel of Figure (4.9) shows the same for model (B). Here the entropy is required to match observations at *both* $0.1r_{200}$ and r_{500}. In the bottom panel, the solid line represents a non-linear relation between the total energy injected to the cluster by AGN and the mass of the cluster (see next section for more details). In the two top panels of Figure (4.9), the solid line represents a linear relation between the energy injected by the AGN, $E_{\rm agn}$ and cluster mass, $M_{\rm cl}$.

Figure (4.10) shows the X-ray luminosity ($L_{\rm X}$ versus emission-weighted temperature ($T_{\rm X}$) relation in clusters for model (B). As we've mentioned before, model (B) is constrained by both entropy versus temperature relation as well as X-ray luminosity versus temperature relation observed in clusters whereas model (A) only follows the constraint of observed entropy versus temperature. The data points have been compiled from Arnaud & Evrard (1999) (represented by stars), Markevitch et al. 1998 (represented by open squares) and Helsdon & Ponman 2000 (with error bars). The X-ray luminosity has been calculated within the cluster volume of $0.3r_{200}$, as done for the data. It is also seen that the X-ray luminosity does not change much (within 1%) if the volume increased from $0.3r_{200}$ to r_{200}. The shaded region in the plot corresponds to the predicted X-ray luminosity when the cluster is heated by an AGN for $5{\times}10^8 \leq t_{\rm heat} \leq 5{\times}10^9$ years with luminosities which correspond to the two bounding lines of the shaded region in the bottom panel of Figure (4.9). It is seen that the predicted luminosities of the heating model satisfy the data points in the low mass end as well as the high mass end. The solid line in the plot shows the predicted luminosity due to the universal temperature profile and the default density profile. We note that the X-ray luminosity is over-predicted by the universal

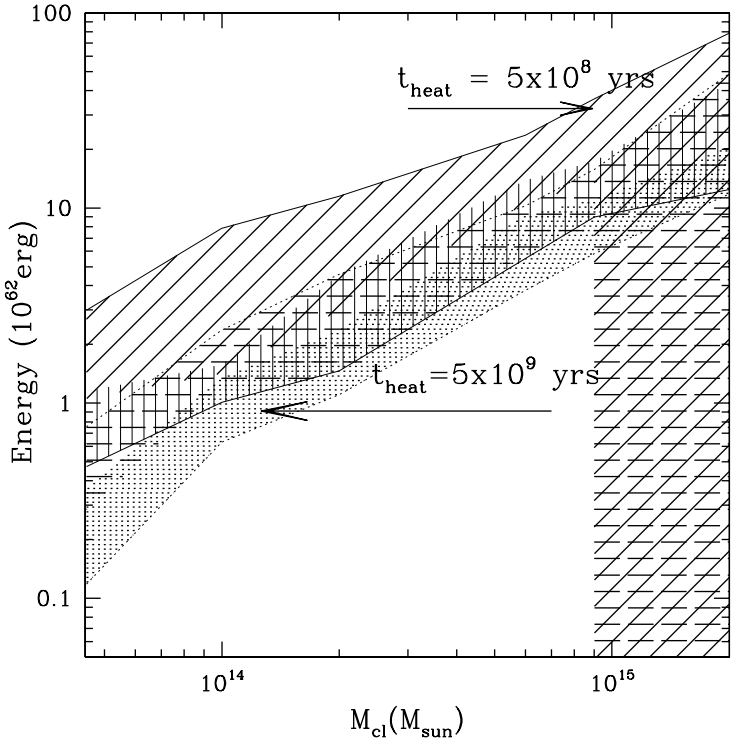

Figure 4.8: Allowed ranges of total injected energy $E_{\rm agn} = \langle L \rangle \times t_{\rm heat}$ required to match the observed entropy at $0.1r_{200}$ and/or r_{500}, for two different values of $t_{\rm heat}$, as a function of cluster mass. The width of each region corresponds to the $1-\sigma$ errors plotted in Figure (4.1). The region bounded by thin solid lines corresponds to the allowed range in energies for $t_{\rm heat} = 5 \times 10^8$ years. Within this bounded region, the area shaded with vertical solid lines is the spread in energy that satisfies the entropy requirement at $0.1r_{200}$ and the area shaded with oblique solid lines is the spread in $E_{\rm agn}$ that satisfies the entropy requirement at r_{500}. Only the overlap region satisfies the observations at both radii. The region bounded by thin dotted lines corresponds to the allowed range in energies for $t_{\rm heat} = 5 \times 10^9$ years. In this region, the dotted area is the spread in energy that satisfies the entropy requirement at $0.1r_{200}$ and the area shaded with horizontal long-dashed lines is the spread in $E_{\rm agn}$ that satisfies the entropy requirement at r_{500}.

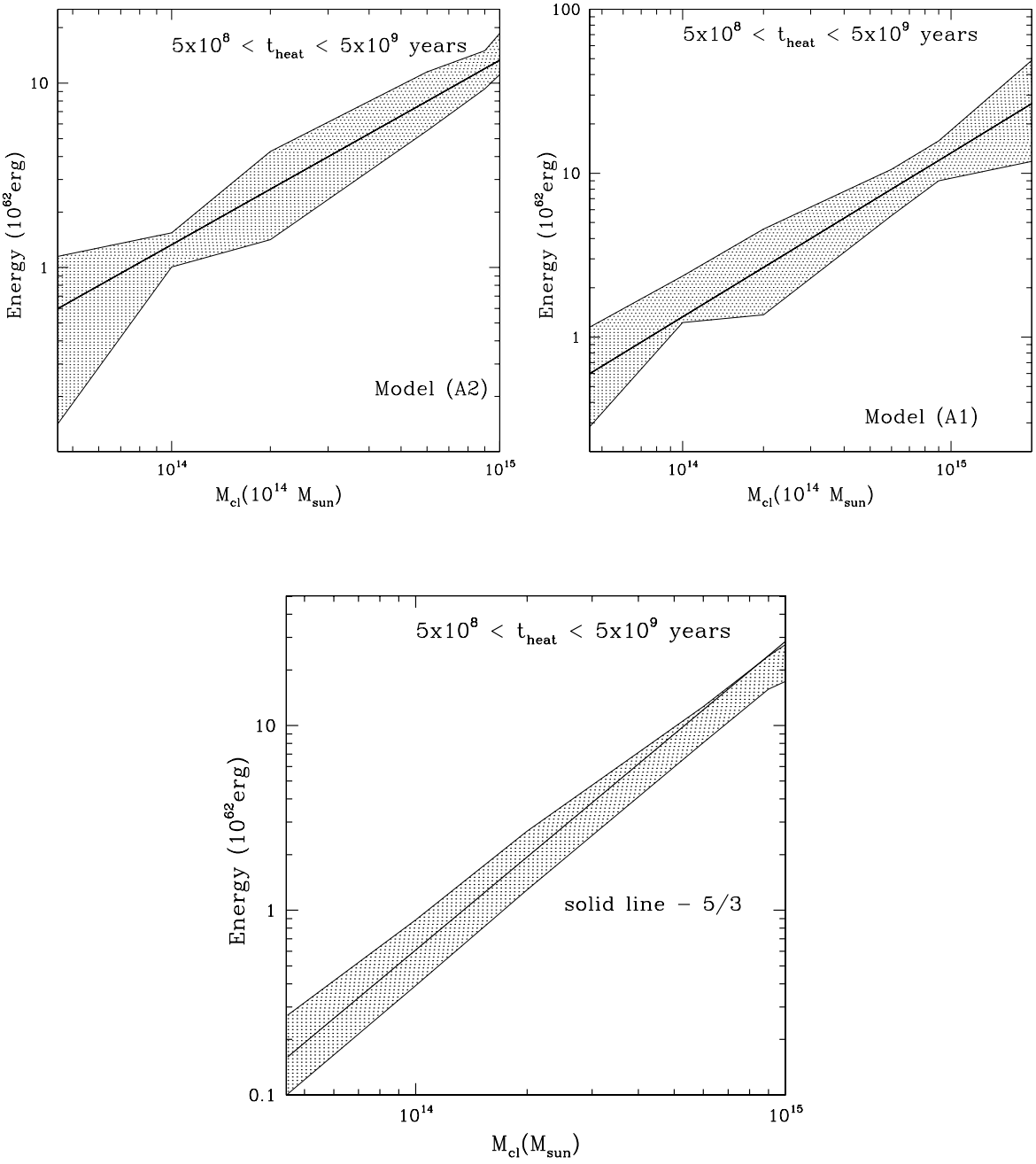

Figure 4.9: These three figures show the permitted total injected energy range as a function of the cluster mass for ICM heating times between $t_{\rm heat} = 5 \times 10^8$yr (upper envelope) and $t_{\rm heat} = 5 \times 10^9$yr (lower envelope) for the three models (A1) (top, left panel), (A2) (top, right panel) and (B) (bottom panel). The shaded region corresponds to values of $E_{\rm agn}$ that are able to match the entropy observations at *both* $0.1r_{200}$ and r_{500}. The solid line in the bottom panel represents a non-linear relation between the total energy injected into the cluster by AGN and the mass of the cluster with an exponent of 5/3 for model (B). The thick solid line in the two top panels represents a linear relation with exponent between the total energy, $E_{\rm agn}$ and the cluster mass, $M_{\rm cl}$. The permitted parameter space comes from the sum of permitted regions that satisfy the entropy constraints at both radii for fixed $t_{\rm heat}$.

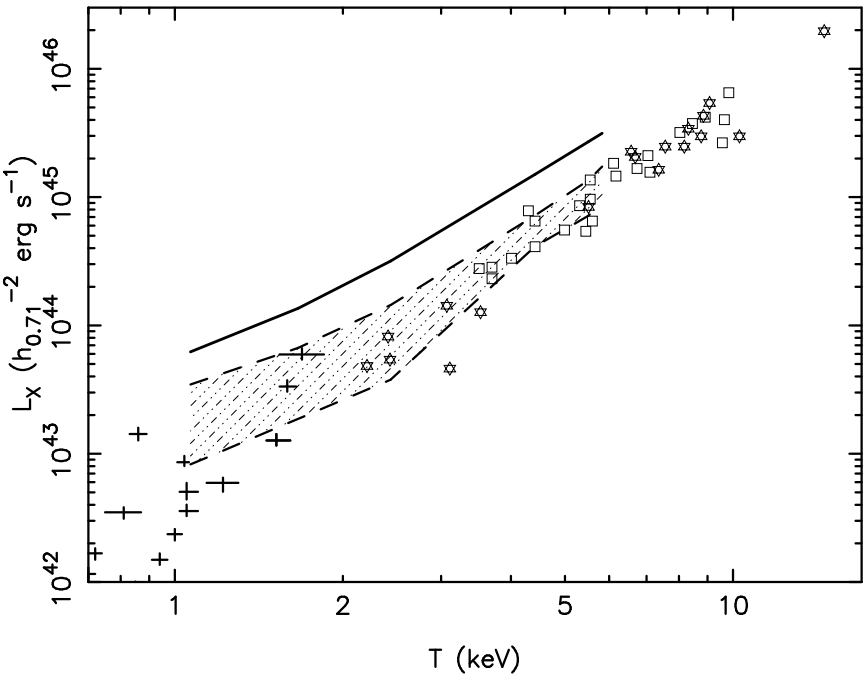

Figure 4.10: Relation between bolometric X-ray luminosity L_X and emission- weighted temperature ($\langle T \rangle$) for model (B) ie. AGN heating with thermal conduction. The data points represented by 'stars' show measurements of clusters with insignificant cooling flows compiled by Arnaud & Evrard (1999). Open squares show cooling flow-corrected measurements by Markevitch et al. (1998). The data points with error bars show group data from Helsdon & Ponman (2000). The shaded region represents X-ray luminosity calculated for the region of $E_{\rm agn}$ shown in Figure (4.9) which satisfies the observed entropy requirements at both radii for $5 \times 10^8 < t_{\rm heat} < 5 \times 10^9$ years. The solid line represents the X-ray luminosity calculated using the default model of the ICM ie. the universal temperature profile. The models assume a ΛCDM cosmology with $\Omega_M = 0.29$, $\Omega_\Lambda = 0.71$, and $\Omega_b = 0.047$, and a Hubble parameter of $h = 0.71$ has been applied to the models and the data.

temperature profile which indicates that the addition of non-gravitational heating is required to lower the X-ray luminosity to satisfy the data points (see chapter (2) for more details).

4.4 The halo-black hole mass relation

The relation between the mass of the group or cluster halo and the total injected energy (Figure (4.9)) can be translated to the halo-black hole mass relation. As an illustrative example of such a relation, the solid line in the bottom panel of Figure (4.9) can be interpreted as a non-linear relation between $E_{\rm agn}$ and $M_{\rm cl}$. This is derived using arguements by Wyithe & Loeb (2003). Since, such non-linear relations between black hole mass and the galaxy velocity dispersion have been derived theoretically in literature as well as in observations (Ferrarese & Merritt (2000)), it to be worth-while to compare if this relation with the relation between cluster mass and black hole, as suggested by our results in the earlier section. Mass of a virialized halo can be expressed in terms of its circular velocity $v_{\rm c}$ (Barkana & Loeb 2001)

$$M_{\rm halo} = 4.7 \times 10^{14} \left(\frac{v_c}{10^3 \text{ km s}^{-1}} \right)^3 M_\odot \tag{4.34}$$

We can combine the above relation with the self-regulation condition (Wyithe & Loeb 2003)

$$\eta L_{\rm Edd} F_q = \frac{0.5(\Omega_b/\Omega_m) M_{\rm halo} v_c^2}{t_{\rm dyn}}, \tag{4.35}$$

where $L_{\rm Edd}$ is the Eddington luminosity of the central black hole, η is its Eddington fraction, F_q is the fraction of energy generated by the black hole that is deposited in the gas, Ω_b and Ω_m are the mass density in baryons and in mass relative to the critical density, respectively. We assumed that the dynamical time of the halo gas is $t_{\rm dyn} \sim r_{\rm vir}/v_c$, where $r_{\rm vir}$ is the virial radius of the collapsed halo (Barkana & Loeb 2001). Combining equations (4.34) and (4.35) we get

$$M_{\rm bh} = 2.2 \times 10^8 \left(\frac{\eta F_q}{0.05} \right)^{-1} M_{14}^{5/3} M_\odot, \tag{4.36}$$

where $M_{14} = M_{\rm halo}/10^{14} M_\odot$. Note that the above relation between the mass of the cluster and the central black hole is nonlinear. It is interesting that a similar scaling would be expected in the case of the galaxy halo mass $M_{\rm gh}$ and black hole mass relation. In such a case, the mass of the black hole scales like $M_{\rm bh} \propto v_c^\alpha$, where $4 \lesssim \alpha \lesssim 5$. As $v_c^2 \propto M_{\rm gh}/r_{\rm gh}$ and $r_{\rm gh} \propto M_{gh}$, we have $M_{\rm bh} \propto M_{\rm gh}^{\alpha/3}$.

Assuming that a fraction ϵ of black hole mass is converted to energy, we can also get the relation between the injected energy $E_{\rm agn}$ and the cluster mass

$$E_{\rm agn} = 6 \times 10^{61} \left(\frac{\epsilon}{0.15} \right) \left(\frac{\eta F_q}{0.05} \right)^{-1} M_{14}^{5/3}. \tag{4.37}$$

This relation is the same as the one denoted by solid line in the bottom panel of Figure (4.9).

We also try to fit the same non-linear relation to model (A1) and (A2). However, we notice that this relation does not provide a good fit to the shaded region in the top, right panel of Figure (4.9). A linear relation is more appropriate in the case of these two models. We however note that the results of

the model of AGN heating with thermal conduction are closer to observations. We therefore interpret the relation between black hole and cluster mass, as suggested by our calculations, to be non-linear.

4.5 Discussions

4.5.1 Models (A1) and (A2)

As is clear from Figure (4.8) and the top two panels of Figure (4.9), it is possible to heat the ICM with a *single* central AGN to match the entropy requirements at *both* $0.1r_{200}$ and r_{500} in model (A). However, in order to match the entropy at both radii, the total injected energy $E_{\rm agn}$, for a given value of $t_{\rm heat} \ll t_{\rm H}$, must be tightly constrained. In fact, our calculations have shown that for any value of $t_{\rm heat} < t_{\rm H}$, i.e., for any heating time (or AGN lifetime), it is always possible to satisfy the entropy observations at *both* radii with a *single* value of the luminosity $\langle L \rangle$. This is different from the cooling flow problem, where $\langle L \rangle$ must be finely tuned to match the cooling rate (Ruszkowski & Begelman 2002), because cooling effects on large scales are rather mild and, thus, the results depend mostly on the total injected energy $E_{\rm agn} = \langle L \rangle \times t_{\rm heat}$. Thus, if we can fit the observed entropy values for just one pair $\langle L \rangle$ and $t_{\rm heat}$, we can do so for a wide range of such pairs. Another manifestation of this fact is that the shaded regions in Figure (4.8) are similar in shape but are just offset by a factor of a few. As the cooling effects are relatively mild, the modest differences arise because shorter heating times lead to higher temperatures and convective transport cannot "catch up" with the energy supply. As the entropy excess to be explained is known from observations and is fixed, more heat has to be injected for shorter heating times. Nevertheless, the results are mostly sensitive to the *total* energy input from the black hole, rather than to $\langle L \rangle$ and $t_{\rm heat}$ separately. As a consequence, satisfactory fits can be obtained as long as the total injected energy falls within a relatively narrow range of values, which depends on the cluster mass (top two panels of Figure (4.9)).

We would like to point out here that the energy required to be supplied by the AGN, $E_{\rm agn}$, is slightly lowered in model (A2) as compared to model (A1) due to the introduction of the smooth core in the NFW profile. This is probably due to the fact that the initial density becomes shallower on introduction of a core in the dark matter distribution reducing the excess entropy requirement at both radii for all $t_{\rm heat}$. In addition, we also point out that the effective heating time may be longer than the integrated AGN lifetimes. Heating of the cluster may occur more gradually as heat gets distributed on a timescale very roughly proportional to the sound crossing time from the cluster center to a given radius. Thus, $t_{\rm heat}$ should be interpreted as an upper limit on the AGN lifetime.

Note that for longer heating times the luminosity constraints become less stringent and lower black hole masses can explain the observed trends. Finally, as we consider heating on large scales, all galaxies in the cluster that go through an active phase will contribute to the overall energy budget of the cluster gas. For example, substructure in the cluster could contain galaxies with sizable bulge components, each of which may contain a supermassive black hole. Therefore, the constraint on the black hole mass obtained above should be interpreted as a sum of all black hole masses that contribute to heating rather than the mass of an individual black hole. This could also lower the required efficiency of individual black holes that contribute to cluster heating.

Finally, we note that cooling and convection play important roles in controlling the heating mech-

anism so that the entropy profiles broadly match the observed entropy profiles in clusters (Ponman et al. 2003). Notably, in the later stages of evolution of the gas, after the heating source is switched off, convection flattens the entropy profiles in the central regions of the cluster. Moreover, an entropy core seems to develop in the final stages of the evolution of the ICM, notably so for model (A1). This is consistent with the observed entropy profiles, which show cores at $r \leq 0.1 r_{200}$ (Ponman et al. 2003). Our entropy profiles do not show steep positive gradients as observed in the entropy profiles of two groups of galaxies (Mushotzky et al. 2003). However, these groups have masses smaller than the ones considered here. In model (A2), the introduction of a smoothened core radius in the dark matter profile almost removes the isentropic core for low mass clusters ($T_{\rm X} < 4$ keV). However, since the temperature profiles show a temperature gradient even though the entropy is flattened (clearly in model (A1)), thermal conduction might be able to conduct heat out from the central regions of the cluster and reduce temperatures there. This will happen at roughly constant pressure and, therefore, central densities will slightly increase. Thus conduction (if not fully suppressed) may help to remove the core in the center (as is seen in Figure (4.3) for model (B)).

4.5.2 Model (B)

In this chapter, we have also examined the effects of effervescent heating by AGN in clusters with thermal conduction and cooling in the context of the excess entropy requirements at large radii. We have also examined the consequences of this heating, cooling and conduction on SZ temperature decrement.

As is clear from bottom panel of Figure (4.9), it is possible to heat the ICM with a *single* central AGN to match the entropy requirements at *both* $0.1 r_{200}$ and r_{500} in this model also. However, in order to match the entropy at both radii, the total injected energy $E_{\rm agn}$, for a given value of $t_{\rm heat} \ll t_{\rm H}$, must be tightly constrained. In fact, our calculations have shown that for any value of $t_{\rm heat} < t_{\rm H}$, i.e., for any heating time (or AGN lifetime), it is always possible to satisfy the entropy observations at *both* radii with a *single* value of the luminosity $\langle L \rangle$. The results depend mostly on the total injected energy $E_{\rm agn} = \langle L \rangle \times t_{\rm heat}$, as is seen in the earlier two models (A1) and (A2). Thus, as mentioned earlier, if we can fit the observed entropy values for just one pair $\langle L \rangle$ and $t_{\rm heat}$, we can do so for a wide range of such pairs.

We note here that the inclusion of thermal conduction brings down the energy which has to be provided by the AGN over its life-time to satisfy the entropy observations at both radii for all heating times as compared to our model (A1) and (A2) ie. AGN heating with convection. In addition, for shorter heating times, the $E_{\rm agn}$ is less or comparable to the energy pumped in for longer heating times. This is in contradiction to our findings in model (A1) and (A2). This happens here because thermal conduction acts as a heating source after the AGN is switched off (for $t_{\rm H} - t_{\rm heat}$) and raises the entropy at large radii (at $r = r_{500}$). The results are mostly sensitive to the *total* energy input from the black hole, rather than to $\langle L \rangle$ and $t_{\rm heat}$ separately. As a consequence, satisfactory fits can be obtained as long as the total injected energy falls within a relatively narrow range of values, which depends on the cluster mass (bottom panel of Figure (4.9)).

Finally, we note that cooling and thermal conduction play important roles in controlling the heating mechanism so that the entropy profiles broadly match the observed entropy profiles in clusters

(Ponman et al. 2003). Notably, in the later stages of evolution of the gas, after the heating source is switched off, conduction removes negative entropy gradients in the central regions of the cluster. Moreover, there is no entropy core seen in the final stages of the evolution of the ICM. Instead we see positive entropy gradients as observed in the entropy profiles of galaxy groups (Mushotzky et al. 2003, Ponman et al. 2003). Unlike previously proposed models, our model predicts that isentropic cores are not an inevitable consequence of preheating. However, the clusters that show isentropic core have also been observed (Ponman et al. 2003). We note that our entropy profiles show a core while the source of heating is active. It is conceivable that the clusters which show entropy cores are being observed during the active phase of the AGN duty cycle.

4.6 Caveats of the models

We note here that our treatment is simplified as we neglect cosmological terms. We now briefly discuss how our results might change if we consider evolution in the cosmological perspective. First, the mass-temperature relation would change and clusters with the same mass at high redshift would be hotter ($T \propto (H(z)/H_0)^{2/3} M^{2/3}$, the redshift dependence in the ΛCDM universe is approximately $T \propto (1+z)^{0.45}$). Second, the shape of dark matter potential will also change ($c \propto 1/(1+z)$). However, clusters observed today ($z = 0$) were most likely formed at $z \leq 0.5$ (Kitayama & Suto 1996, their Fig. 1). This also depends on the definition of "formation", and the cluster formation will take place at a lower redshift if one defines a cluster to have 'formed' when 75% of its total mass is in place (and not when 50% is in place, assumed by Kitayama & Suto 1996; see e.g, Balogh et al. 1999). More importantly, the higher is the redshift at which AGN injection takes place (AGN could switch on even before the cluster formation redshift as defined above), the lower is the excess entropy to be accounted for. Thus, lower energy injection could be required to explain observations at $z \sim 0$.

We also note that the hydrodynamics equations have been integrated up to r_{200}. It is likely that the buoyant energy transport would be inhibited by the cluster accretion shock at such large radii. However, excess entropy used to constrain our model is measured at smaller radii and we do not expect this to affect our results significantly.

Our simulations assume that heating is instantaneous. This is an approximation as there should be a delay between the onset of AGN activity and heating at a given radius. We have chosen the shortest heating duration to be at least the sound crossing time (or the dynamical time of rising bubbles) at the outer radius where we compare the computed and observed entropies (r_{500}). Thus, for the shortest heating time, our assumption at $0.1 r_{200}$ should be quite reasonable but at r_{500} it would be less accurate but still physically conceivable. For longer heating times our results at both radii should not be affected by this approximation.

Related is the issue of the constraints on the source luminosity. For shorter heating times, higher luminosities are required to assure the same energy injection. This issue is very important in the first two models (A1) and (A2) where there is no thermal conduction. The required luminosities are seen to be more feasible for longer heating times in models (A1) and (A2). However, this problem is reduced on inclusion of thermal conduction in model (B). This happens because thermal conduction acts as a heating source for large radii ($r > 0.5 r_{\rm vir}$). Thus the energy required from the central AGN to reconcile with the observed excess entropy, specially at r_{500}, goes down. In this context, we also note that if the

heating is supplied by more than one AGN, then the luminosity requirements on an individual source would be lower. We also reiterate the point made earlier that if the effects of cosmological evolution had been fully taken into account and AGN had supplied heating at earlier epochs, then the energy requirements presented here would have been further reduced. Thus, the source luminosities would also be lower for a given heating time. This is due to the fact that the required excess entropy at higher redshift would be reduced.

Finally, in these models, we do not include the effects of magnetic fields explicitly. However, magnetic fields are likely to be below the equipartition value and thereby dynamically unimportant (Fabian et al. 2002). Polarization measurements suggest that the magnetic fields in the vicinity of bubbles have subequipartition values (Blanton et al. 2003). Nevertheless, they may still be important for suppressing instabilities on bubble-ICM interfaces. Such effects may implicitly be included in the bubble heating model.

4.7 Conclusions

In this chapter, we have studied whether "effervescent heating" of cluster gas by a central AGN can resolve the entropy problem in clusters of galaxies. We have dealt with three different models here of AGN heating: one where the cluster has a pure NFW dark matter profile and there is AGN heating, where no energy loss due to bubble creation is considered, radiative cooling and convection (model (A1)), the second model (A2) where the cluster has a NFW dark matter distribution with a central core, r_c, and there is AGN heating, where energy loss due to bubble creation are taken in account, radiative cooling and convection and the third one where AGN heating has been combined with thermal conduction and radiative cooling and all the other features of model (A2) have been retained (model (B)).

In models (A1) and (A2), the AGN (or a group of AGNs in the central region) injects bubbles of buoyant gas, which heat the ICM. The mean volume heating rate due the bubbles is a function of the ambient pressure and a time-averaged energy injection rate to the ICM, but not of the detailed properties of the bubbles or their evolution. We have also included the effects of radiative cooling and convection. We assumed that heating continues for $t_{\rm heat}$, the duration of heating, and have studied the resulting evolution of the gas assuming it to be in quasi-hydrostatic equilibrium for the Hubble time. The only free parameters of this model are $\langle L \rangle$, the energy injection rate to the ICM, and $t_{\rm heat}$. The main results of our study are summarized as follows:

1. We find that there are allowed values of $\langle L \rangle$ for which it is possible to match the entropy observations of clusters even at large radii (both $0.1r_{200}$ and r_{500}) with a *single* central AGN for a large range of $t_{\rm heat}$ ($5 \times 10^8 \leq t_{\rm heat} \leq t_{\rm H}$ years) and cluster masses ($5\times10^{13} - 2\times10^{15}{\rm M}_\odot$). The energy requirement is lowered slightly on introduction of a core in the dark matter profile.

2. Convection plays an important role in removing negative entropy gradients produced by heating in the central regions of the cluster.

3. The results are mostly sensitive to the total energy $E_{\rm agn}$ injected into the cluster by AGN (as cooling effects are relatively mild). The model predicts that the total injected energy

$E_{\rm agn} = \langle L \rangle \times \Delta t$, required to satisfy observational entropy constraints, should be correlated with the cluster mass.

In model (B), the primary aim was to study the implications AGN heating and thermal conduction on the global properties of groups and clusters of galaxies. We also set out to examine what differences would the introduction of thermal conduction make in the results as compared to our models (A1) and (A2) where there was convection along with "effervescent heating".

The main results of this model (B) are summarized below:

1. We have demonstrated that the available entropy data, in conjunction with our feedback model, put constraints on the relation between the total energy injected by the AGN and the mass of the cluster. The inferred black hole-halo mass scaling ($M_{bh} \propto M^{\alpha}_{\rm cluster}$, $\alpha \sim 1.5$) is an analog and extension of the similar relation between the black hole mass and the mass of the galaxy halo that holds on smaller scales.

2. Unlike in the case of previously proposed models, we find that isentropic cores are not an inevitable consequence of preheating. This is consistent with observations of groups that do not show large isentropic cores (Ponman et al. 2003, Mushotzky 2003). Clusters that show isentropic core have also been observed (e.g., Ponman et al. 2003). We note that our entropy profiles show a core while the source of heating is active which may explain such cases as well. It is conceivable that the clusters which show entropy cores are being observed during the active phase of the AGN duty cycle.

4. We find that the inclusion of thermal conduction removes the negative gradient in the temperature profiles in the central regions of clusters and make them more physical.

3. We have also demonstrated that the model reproduces the observed trend for the density profiles to flatten in low mass systems.

Bibliography

Afshordi N. & Cen R., 2002, ApJ, 564, 669

Allen S. W. et al. , 2001, MMRAS, 324, 842

Babul A., Balogh M. L., Lewis G. F., & Poole G. B., 2002, MNRAS, 330, 329

Balogh, M. L., Babul, A., & Patton, D. R, 1999, MNRAS, 307, 463

Basson J. F. & Alexander P. 2003, MNRAS, 339, 353

Barkana, R., & Loeb, A., 2001, Physics Reports, 349, 125

Binney J. & Tabor G., 1995, MNRAS, 276, 663

Begelman M. C., 2001, in Gas and Galaxy Evolution, APS Conf. Proc., vol. 240, ed. Hibbard, J. E., Rupen M. P., van Gorkom J. H., p. 363, (astro-ph/0207656)

Blanton E. L., Sarazin C. L., McNamara B. R., & Wise M. W., 2001, ApJ, 558, 15

Blanton E. L., Sarazin C. L., & McNamara B. R., 2003, ApJ, 585, 227

Brüggen M., 2003a, ApJ, 593, 700

Brüggen M., 2003b, ApJ, 592, 839

Bryan G. L., 2000, ApJ, 544, 1

Bullock J. S. et al. , 2001, MNRAS, 321, 559

Chandran, B., & Maron, J., 2004, ApJ, 602, 170

Churazov E. et al. , 2001, ApJ, 554, 261

Clarke D. A., Norman M. L., & Fiedler, R. A. 1994, ZEUS-3D User's Manual Version 3.2.1, (Urbana-Champaign: Univ. Illinois)

Croston, J.H., Hardcastle, M.J. & Birkinshaw, M., 2005, MNRAS, 357, 279

Davé R., Katz N., & Weinberg D. H., 2002, ApJ, 579, 23

Donahue, M., 2005, conference talk at "The Future of Cosmology with Clusters of Galaxies", Feb 26 – Mar 2 2005, Kona, Hawaii, talk published online at http://www.umich.edu/ mctp/future/program.html

Ettori S., 2003, MNRAS, 344, 13

Fabian A. C. et al. , 2000, MNRAS, 318, 65

Fabian, A.C., Celotti, A., Blundell, K.M., Kassim, N.E., & Perley, R.A., 2002, MNRAS, 331, 369

Ferrarese L., & Merritt D., 2000, ApJ, 539, 9

Finoguenov A., Reiprich T. H., & Böhringer H., 2001, A&A, 368, 749

Gardini, A., & Ricker, 2004, Mod. Phys. Lett., A19, 2317

Gebhardt K., et al. , 2000, ApJ, 543, 5

Heinz S., Choi Y., Reynolds, C. S., & Begelman M. C., 2002, ApJ, 569, 79

Johnstone R. M., Allen S. W., Fabian A. C., & Sanders J. S., 2002, MNRAS, 336, 299

Kaiser C. R., & Binney J., 2003, MNRAS, 338, 837

Kitayama T. & Suto Y., 1996, ApJ, 469, 480

Komatsu, E., & Seljak, U. 2001, MNRAS, 327, 1353

Lloyd-Davies E. J, Ponman T. J., Cannon D. B., 2000, MNRAS, 315, 689

Loeb, A. 2002, New Astronomy, 7, 279

Loken C., Norman M.L., Nelson E., Bryan G.L., & Motl P., 2002, ApJ, 579, 571

Magorrian J. et al. , 1998, AJ, 115, 2285

Mazzotta P. et al. , 2002, ApJ, 567, 37

McNamara B.R. et al. , 2000, ApJ, 534, 135

McNamara B.R. et al. 2001, ApJ, 562, 149

Muanwong O., Thomas P. A., Kay S. T., & Pearce F. R., 2002, MNRAS, 336, 527

Mushotzky R. et al. , 2003, American Astronomical Society, HEAD meeting, 35, 13.07 (astro-ph/0302267)

Narayan, R., & Medvedev M.V., ApJ, 562, 129

Nath B. B., 2003, MNRAS, 339, 729

Nath B. B., & Roychowdhury S., 2002, MNRAS, 333, 145

Omma et al. , 2004, MNRAS, 348, 1105

Omma H., & Binney, J., 2004, MNRAS, 350, 13

Pratt G. W., & Arnaud M., 2003, A&A, 408, 1

Pratt G. W., Arnaud M., 2005, A&A, 429, 1

Ponman T. J., Sanderson A. J. R., & Finoguenov A., 2003, MNRAS, 343, 331

Peebles P. J. E., 1980, The Large Scale Structure of the Universe, Princeton Univ. Press, Princeton, NJ

Peterson J. R. et al. , 2001, A&A, 365, 104

Quilis V., Bower R. G., & Balogh, M. L., 2001, MNRAS, 328, 1091

Reynolds C. S., Heinz S., & Begelman M. C., 2002, MNRAS, 332, 271

Roychowdhury S., & Nath B. B., 2003, MNRAS, 346, 199

Ruszkowski M., & Begelman M. C., 2002, ApJ, 581, 223

Ruszkowski M., Brüggen M., & Begelman M. C., 2004, ApJ, 611, 158

Sanderson, A.J.R., Ponman, T.J., Finoguenov A., Lloyd-Davies, E.J., & Markevitch, M., 2003, MNRAS, 340, 989

Shapiro, P.R., Iliev, I,T., 2000, ApJ, 542, 1

Stone J. M., Pringle J. E., & Begelman M. C., 1999, MNRAS, 310, 1002

Sutherland R. S., & Dopita M. A., 1993, ApJS, 88, 253

Tabor G., & Binney J., 1993, MNRAS, 263, 323

Tornatore L., Borgani S., Springel V., Matteucci F., Menci, N., & Murante G., 2003, MNRAS, 342, 1025

Tyson, J.A., Kochanski, G.P., Dell' Antonio, 1998, ApJ, 498, 107

Murante G., 2003, MNRAS, 342, 1025

Tozzi P., & Norman C., 2001, ApJ, 546, 63

Valageas P., & Silk J., 1999, A&A, 350, 725

Voit G. M., & Bryan G. L., 2001, Nature, 414, 425

Wu K. K. S., Nulsen P. E. J., & Fabian A. C., 2000, MNRAS, 318, 889

Wu X., & Xue Y., 2002, ApJ, 572, 19

Wyithe J. S., & Loeb A., 2003, ApJ, 595, 614

Zakamska, N.L., Narayan, R., 2003, ApJ, 582, 162